vibration

MDPI

Article

How Far Should Poles Be Placed? Selecting Positive Feedback Controllers for Damping and Tracking Applications: A Complete Characterisation

James MacLean †, Majid Aleyaasin † and Sumeet S. Aphale *,†

School of Engineering, University of Aberdeen, Aberdeen AB24 3FX, UK
* Correspondence: s.aphale@abdn.ac.uk
† These authors contributed equally to this work.

Abstract: Designers of Positive Feedback Controllers (PFCs) arbitrarily place poles into the left-hand half-plane of the complex plane without any detailed understanding of where to stop. This works aims to clearly demonstrate, via rigorous mathematical derivation, the conditions for which pole–placement becomes possible. It also highlights the design limits for the family of second–order PFCs—the most popular PFC group. To this end, the complete family of PFCs, namely, Positive Acceleration Velocity Position Feedback and its derivatives, are analysed in great depth with respect to pure damping and also with respect to combined damping and tracking applications. To showcase the practical value and validity of this work, experimental results on a piezoelectric nanopositioner are also presented and discussed.

Keywords: positive–feedback–control; PAVPF; PVPF; PPF; resonance; optimisation; damping

check for updates

Citation: MacLean, J.; Aleyaasin, M.; Aphale, S.S. How Far Should Poles Be Placed? Selecting Positive Feedback Controllers for Damping and Tracking Applications: A Complete Characterisation. *Vibration* **2022**, *5*, 641–658. https://doi.org/10.3390/vibration5040038

Academic Editor: Evgeny Petrov

Received: 4 August 2022
Accepted: 7 September 2022
Published: 20 September 2022

Publisher's Note: MDPI stays neutral with regard to jurisdictional claims in published maps and institutional affiliations.

Copyright: © 2022 by the authors. Licensee MDPI, Basel, Switzerland. This article is an open access article distributed under the terms and conditions of the Creative Commons Attribution (CC BY) license (https://creativecommons.org/licenses/by/4.0/).

1. Introduction

Resonance-induced vibrations are a major cause of concern and a rigid limiting factor in the design and operation of many technological systems [1]. Consequently, substantial research effort has been channelled in this direction, leading to several passive and active resonance-damping techniques being reported [2–4]. Due to their superior performance, high-tunability and robust performance under parameter uncertainties, active closed–loop damping schemes have been favoured over their passive open–loop counterparts [5,6]. Integral Force Feedback, Integral Resonant Control, Velocity feedback, Active Shunt damping, Resonant controllers and Robust Control have all been reported to deliver excellent damping performance [7–12]. All these controllers are implemented in the standard negative feedback.

Another family of second–order damping controllers that are typically implemented in a positive feedback configuration are also equally popular. This group consists of the Positive Position Feedback (PPF), the Positive Velocity Position Feedback (PVPF) and Positive Acceleration Velocity Position Feedback (PAVPF) [13–16]. Successful application of these Positive Feedback Controllers (PFCs) is well-documented throughout relevant literature. These controllers have been employed predominantly to damp system resonances where a lightly-damped resonant mode at relatively low frequencies ($\leq$1 kHz) dominates the overall dynamics, and the higher–frequency modes are sufficiently far away from the first mode. Examples of such systems are piezoelectric–tube nanopositioners, nanopositioning platforms, high–density memory storage devices, aerospace structures, flexible manipulators, cantilever beams, civil structures, disc drive actuators, etc. [17–21].

Though these PFCs are popular and show adequate robustness under parameter uncertainties, their design is based on pole–placement via trial–and–error. As such, a systematic design strategy or optimisation of the controller design against certain application–specific indices has remained elusive. Consequently, the selection of closed–loop pole locations that

deliver optimum damping performance has proved difficult. It is also noticed in several cases that increased damping comes at the cost of increased closed–loop DC sensitivity. In many applications such as precision micro– and nanopositioning, increased DC sensitivity is undesirable but inherently unavoidable if PFCs are employed for damping [22]. Consequently, a systematic method of optimising these popular pole–placement–based PFCs has the potential to positively impact a wide range of technological systems.

In this work, all second–order PFCs, namely the PPF, PVPF and PAVPF controllers, are parametrically analysed for maximising closed–loop damping with respect to closed–loop DC sensitivity (DC gain), thereby allowing for the selection of an optimal solution that satisfies the combination of the aforementioned. It is crucial to note that DC sensitivity and DC gain are synonyms for each other in this context. If the DC gain increases, the sensitivity to low–frequency noise thereby increases, thus affecting system performance. Conversely, if the DC gain decreases, then attenuation of all frequencies occurs, which thereby attenuates the desired output from said system. It is crucial to highlight in this work that when the phrase "DC sensitivity is minimised" is used, it is akin to saying that the "DC gain is brought as close to zero as possible".

In addition, each PFC is put in closed–loop with an integral tracking controller and optimised with respect to controller bandwidth using the -3.01 dB point. A method of systematically designing any of the three second–order positive feedback controllers for optimum performance in terms of closed–loop damping achieved and closed–loop DC sensitivity is presented. The novelty in this paper consists of the following;

1. Full parametric analysis of the PFC family,
2. Inform the selection of an optimal solution for each of these controllers with respect to maximising closed–loop damping and keeping the DC gain as close to zero (minimising DC sensitivity) simultaneously,
3. The analysis and design of an optimal tracking controller for each type of controller for combined tracking and damping applications in which tracking bandwidth is maximised,
4. Definitive guidelines for the selection of positive feedback controllers for damping, as well as combined damping and tracking applications.

The paper is constructed as follows; Section 2 introduces the open–loop system and then details the closed–loop equations for PAVPF control, which leads to the matrix equations involved with optimal gain selection, Section 4 details the optimisation of PPF with detailed closed–loop results, Section 5 details the optimisation of PVPF with detailed closed–loop results, Section 6 details the optimisation of PAVPF when designed in a mathematically overdetermined manner, Section 7 details the optimisation of PAVPF in a mathematically determined manner and draws conclusions compared to the prior mentioned, and lastly, Section 8 draws important remarks and conclusions about the controller family as a whole.

2. Preliminaries

In general, systems such as nanopositioners, flexible robotic manipulators, sensors and disc drives can are collocated by nature and can be generally modelled by a series of infinite second–order resonant transfer functions as follows:

$$\bar{G}(s) = \sum_{i=1}^{\infty} \frac{\gamma_i^2}{s^2 + 2\zeta_i \omega_i s + \omega_i^2}, \tag{1}$$

where γ_i^2/ω_i^2 is the DC gain, ζ_i is the damping ratio and ω_i is the resonant frequency of the ith resonant modes, respectively, such that $\omega_i < \omega_{i+1} \forall \omega_i$. To simplify the system, it is important to note that the first resonant mode is dominant and usually separated far away from the higher resonant modes [23,24]. It has also been noted that if left undamped, this highly-dominant first resonant mode enforces severe limitations on the operational safety, as well as positioning performance of the aforementioned systems. Consequently, most techniques focus on damping this first resonant mode, and subsequent controller designs

are based on a plant model, consisting of a second–order transfer-function (accounting for the dominant resonant mode) [25] and an adequate feed–through term (accounting for the truncation of the higher–order dynamics) [26]. The simplification for (1) is as follows:

$$G(s) = \frac{\gamma_1^2}{s^2 + 2\zeta_1\omega_1 s + \omega_1^2} + d_{f1}, \tag{2}$$

where γ_1, ω_1 and ζ_1 are the first resonant mode numerator constant, resonant frequency, damping ratio, respectively, and d_f is the feed–through term, which accounts for truncation effects. In order to dampen the dominant resonant mode of such systems, a family of positive feedback controllers have been developed, namely PPF (Positive Position Feedback) [27], PVPF (Positive Velocity Position Feedback) [22], PAVPF (Positive Acceleration Velocity Position Feedback) [16] and IRC (Integral Resonant Control) [23]. In this work, the primary focus is the positive feedback controller consisting of PPF through to PAVPF. Consider the following definition for PAVPF control;

$$C(s)_{\text{PAVPF}} = \frac{\Gamma_0 s^2 + \Gamma_1 s + \Gamma_2}{s^2 + \Gamma_3 s + \Gamma_4}, \tag{3}$$

where $\Gamma_i \forall \{i \in \mathbb{Z} | i \in [1,4]\}$ are controller gains to be determined. To derive the PPF and PVPF controllers, all that is required is to set Γ_0 and Γ_1 and Γ_0 to zero, respectively, for the controller of interest in Equation (3);

$$C(s)_{\text{PPF}} = \frac{\Gamma_2}{s^2 + \Gamma_3 s + \Gamma_4}, \tag{4}$$

$$C(s)_{\text{PVPF}} = \frac{\Gamma_1 s + \Gamma_2}{s^2 + \Gamma_3 s + \Gamma_4}. \tag{5}$$

Figure 1 shows the general closed–loop configuration structure for damping (**a**) and damping with tracking (**b**) respectively. Since this family of controllers are damping–focused, the central design criteria are to bring the closed–loop damping as close to one as possible. To this end, the most important gains to optimise are Γ_0, Γ_1 and Γ_2, respectively. A secondary but equally important performance index to consider is the DC sensitivity. It is most desirable to impart maximum damping to the resonant mode without forcing any change to the overall system's DC sensitivity. Though this has remained elusive in most positive feedback implementations documented in the relevant literature, this exercise aims at categorically proving that such a design cannot be achieved in the PPF case and proposes designs for PVPF as well as PAVPF where both performance indices (high damping coefficient and unchanged DC sensitivity) are adequately met. Consider putting Equation (3) in positive feedback with Equation (2):

$$G_{\text{CL}}(s) = \frac{G(s)}{1 - G(s)C(s)_{\text{PAVPF}}}. \tag{6}$$

The closed–loop equation can be summarised as:

$$G_{\text{CL}}(s) = \frac{D_4 s^4 + D_3 s^3 + D_2 s^2 + D_1 s + D_0}{s^4 + C_3 s^3 + C_2 s^2 + C_1 s + C_0}, \tag{7}$$

where the denominator and numerator coefficients are shown in Tables 1 and 2.

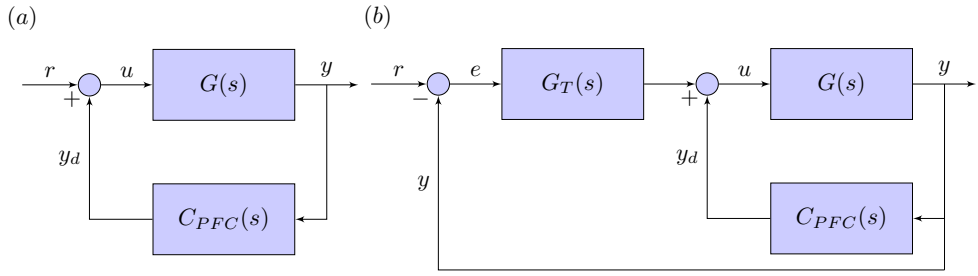


Figure 1. Block diagram structures for damping (**a**) and damping with tracking (**b**), respectively. Here, r, e, u, y and y_d represent the reference, error, control input, output and modified output, respectively. $G_T(s)$, $G(s)$ and $C_{PFC}(s)$ are the tracking controller, plant and positive feedback controller, respectively.

Table 1. Denominator coefficient table.

Coeff	**Terms**
C_3	$2\zeta_1\omega_1 + \dfrac{\Gamma_3 - d_{f1}\Gamma_1}{1 - d_{f1}\Gamma_0}$
C_2	$\omega_1^2 + \dfrac{2\zeta_1\omega_1\left(\Gamma_3 - d_{f1}\Gamma_1\right) + \Gamma_4 - d_{f1}\Gamma_2 - \gamma_1^2\Gamma_0}{1 - d_{f1}\Gamma_0}$
C_1	$\dfrac{2\zeta_1\omega_1\left(\Gamma_4 - d_{f1}\Gamma_2\right) + \omega_1^2\left(\Gamma_3 - d_{f1}\Gamma_1\right) - \gamma_1^2\Gamma_1}{1 - d_{f1}\Gamma_0}$
C_0	$\dfrac{\omega_1^2\Gamma_4 - \left(d_{f1}\omega_1^2 + \gamma_1^2\right)\Gamma_2}{1 - d_{f1}\Gamma_0}$

Table 2. Numerator coefficient table.

Coeff	**Terms**
D_4	d_{f1}
D_3	$\dfrac{d_{f1}(\Gamma_3 + 2\zeta_1\omega_1)}{1 - d_{f1}\Gamma_0}$
D_2	$\dfrac{d_{f1}\left(\Gamma_4 + \omega_1^2 + 2\zeta_1\omega_1\Gamma_3\right) + \gamma_1^2}{1 - d_{f1}\Gamma_0}$
D_1	$\dfrac{d_{f1}\left(\omega_1^2\Gamma_3 + 2\zeta_1\omega_1\Gamma_4\right) + \gamma_1^2\Gamma_3}{1 - d_{f1}\Gamma_0}$
D_0	$\dfrac{\left(d_{f1}\omega_1^2 + \gamma_1^2\right)\Gamma_4}{1 - d_{f1}\Gamma_0}$

From this point, the ideal pole–placement methodology is discussed and demonstrated. Consider an ideal fourth–order, the closed–loop system whose poles are given by:

$$P_1, P_2 = -\sigma_d \pm j\omega_d \quad \text{and} \quad P_3, P_4 = -\sigma_d \pm j\omega_d. \tag{8}$$

These repeated poles are chosen such that their damping is identical, which allows for easy computation and easy comparison with actual imparted closed–loop damping.

Then the desired characteristic polynomial $P_d(s)$ that has the roots given by Equation (8) is defined as:

$$P_d(s) = s^4 + 4\sigma_d s^3 + \left(6\sigma_d^2 + 2\omega_d^2\right)s^2 + 4\sigma_d\left(\sigma_d^2 + \omega_d^2\right)s + \left(\sigma_d^2 + \omega_d^2\right)^2, \tag{9}$$

$$P_d(s) = s^4 + C'_{d3}s^3 + C'_{d2}s^2 + C'_{d1}s + C'_{d0} \tag{10}$$

In order to perform pole–placement between the desired polynomial (10) and the coefficients defined in Table 1, they are set equal to one another as follows;

$$C_0 = C'_{d0}, \quad C_1 = C'_{d1}, \quad C_2 = C'_{d2}, \quad C_3 = C'_{d3}. \tag{11}$$

To this end, the denominator coefficients seen in Table 1 are rewritten in terms of a system of matrix equations. The method is based on nonlinear optimisation, in which a sophisticated objective function, as seen in Equation (16), is comprised of Equations (14) and (15). It should be noted that the objective function originates from matrixial representation (12) of the characteristic polynomial in a closed–loop system. A vector of the controller variables, $\Gamma \in \mathbb{R}^{4\times1}$ is formed, and then the system of equations corresponding to this isolated vector is formed as follows;

$$\begin{bmatrix} -d_{f1} & 0 & 1 & 0 \\ -2\zeta_1\omega_1 d_{f1} & -d_{f1} & 2\zeta_1\omega_1 & 1 \\ -\left(d_{f1}\omega_1^2 + \gamma_1^2\right) & -2\zeta_1\omega_1 d_{f1} & \omega_1^2 & 2\zeta_1\omega_1 \\ 0 & -\left(d_{f1}\omega_1^2 + \gamma_1^2\right) & 0 & \omega_1^2 \end{bmatrix} \begin{bmatrix} \Gamma_1 \\ \Gamma_2 \\ \Gamma_3 \\ \Gamma_4 \end{bmatrix} = \begin{bmatrix} \left(C'_{d1} - 2\zeta_1\omega_1\right)\left(1 - d_{f1}\Gamma_0\right) \\ \left(C'_{d2} - \omega_1^2\right)\left(1 - d_{f1}\Gamma_0\right) + \gamma_1^2\Gamma_0 \\ C'_{d3}\left(1 - d_{f1}\Gamma_0\right) \\ C'_{d4}\left(1 - d_{f1}\Gamma_0\right) \end{bmatrix}, \tag{12}$$

or more compactly:

$$A\Gamma = C, \tag{13}$$

such that $A \in \mathbb{R}^{4\times4}$ and $C \in \mathbb{R}^{4\times1}$. Since the desired pole locations are set through the coefficients of the desired characteristic polynomial (10) as defined in (11), this means that the only set of unknowns is that of the controller variable vector Γ in the system of Equation (12). This numerically implies for a specific Γ_0 set that solving this system of matrices yields the optimal Γ vector for all other controller variables, not including Γ_0. As a result, to optimise the controller in the case of PAVPF, a simple numerical sweep for Γ_0, combined with solving this system of matrices for each Γ_0 chosen, will yield the optimal set of gains based on the performance metrics chosen, namely; maximising closed–loop damping while keeping DC sensitivity minimal or rather keeping the DC gain as close to zero as possible. More specifically, if the closed–loop damping ratio is computed from Equation (8) as:

$$\zeta_{cl}(\sigma_d) = \cos\left(\arctan\left(\frac{\omega_d}{\sigma_d}\right)\right), \tag{14}$$

and the DC gain can be computed by the following:

$$G_{dB}(\sigma_d, \Gamma_0) = 20\log_{10}\left(\frac{\left(d_{f1}\omega_1^2 + \gamma_1^2\right)\Gamma_4(\sigma_d, \Gamma_0)}{\omega_1^2\Gamma_4(\sigma_d, \Gamma_0) - \left(d_{f1}\omega_1^2 + \gamma_1^2\right)\Gamma_2(\sigma_d, \Gamma_0)}\right). \tag{15}$$

As a result of requiring a numerical search, the controller vector $\Gamma(\sigma_c, \Gamma_0)$ becomes a function of the real part of the poles as well as the Γ_0 chosen. The overall optimisation goal for damping applications can be summarised as follows:

$$\max\{\zeta_{cl}(\sigma_d) \mid G_{dB}(\sigma_d, \Gamma_0) \to 0\}. \tag{16}$$

In the following sections to come, the matrix system of Equation (12) and the desired characteristic polynomial (10) provide the basis for the optimisation of all respective controllers. The next subsection details the optimisation procedure for applying integral tracking to PAVPF control and hence PVPF and PPF, respectively.

Integral Tracking Optimisation

Within the context of optimising for both combined damping and tracking applications, the primary optimisation goal is that of maximising the controller bandwidth, namely the -3.01 dB point. To incorporate tracking control to the closed–loop system described by Equation (7), firstly consider the following basic integrator with gain K:

$$G_{\mathrm{T}}(s) = \frac{K}{s}. \tag{17}$$

The new closed–loop equation with integral tracking can be derived by applying Equation (7) in negative feedback with Equation (17) as follows:

$$G_{\mathrm{CL,T}}(s) = \frac{G_{\mathrm{T}}(s)G_{\mathrm{CL}}(s)}{1 + G_{\mathrm{T}}(s)G_{\mathrm{CL}}(s)}. \tag{18}$$

In order to optimise damping and maximise control bandwidth, the integral gain K needs to be optimised such that both of these factors are considered simultaneously. To this end, it is required that:

$$\|G_{\mathrm{CL,T}}(j\omega)\|^2 \leq 1. \tag{19}$$

This ensures that for no possible frequency ω, the closed–loop system response exceeds that of 0 dB, ensuring maximum damping, as well as maximising the -3.01 dB bandwidth of the closed–loop system, which ensures better tracking performance. To optimise K, $G_{\mathrm{CL,T}}(j\omega)$ must be derived. Begin by substituting $s = j\omega$ into (18), gathering real and imaginary terms, which results in:

$$G_{\mathrm{CL,T}}(j\omega) = \frac{K\left[\left(D_4\omega^4 - D_2\omega^2 + D_0\right) + j\left(D_1\omega - D_3\omega^3\right)\right]}{\left[(KD_4 + C_3)\omega^4 - (KD_2 + C_1)\omega^2 + KD_0\right] + j\left[\omega^5 - (KD_3 + C_2)\omega^3 + (KD_1 + C_0)\omega\right]}, \tag{20}$$

then computing $\|G_{\mathrm{CL,T}}(j\omega)\|^2$:

$$\|G_{\mathrm{CL,T}}(j\omega)\|^2 = \frac{K^2\left[\left(D_4\omega^4 - D_2\omega^2 + D_0\right)^2 + \left(D_1\omega - D_3\omega^3\right)^2\right]}{\left[(KD_4 + C_3)\omega^4 - (KD_2 + C_1)\omega^2 + KD_0\right]^2 + \left[\omega^5 - (KD_3 + C_2)\omega^3 + (KD_1 + C_0)\omega\right]^2}, \tag{21}$$

by using the inequality presented in (19), expanding (21) results in a 10th–order polynomial in ω as follows:

$$\|G_{\mathrm{CL,T}}(j\omega)\|^2 = K^2\frac{\bar{V}\omega^8 + \bar{W}\omega^6 + \bar{X}\omega^4 + \bar{Y}\omega^2 + \bar{Z}}{\omega^{10} + \bar{A}\omega^8 + \bar{B}\omega^6 + \bar{C}\omega^4 + \bar{D}\omega^2 + \bar{E}} \leq 1, \tag{22}$$

where the coefficients can be seen as follows in Table 3 and Table 4 respectively.

Table 3. Numerator optimisation coefficients.

Coeff	Terms
$\bar{V}$	D_4^2
$\bar{X}$	$D_3^2 - 2D_4D_2$
$\bar{W}$	$D_2^2 + 2D_4D_0 - 2D_3D_1$
$\bar{Y}$	$D_1^2 - 2D_2D_0$
$\bar{Z}$	D_0^2

Table 4. Denominator optimisation coefficients.

Coeff	Terms
$\bar{A}$	$(KD_4 + C_3)^2 - 2(KD_3 + C_2)$
$\bar{B}$	$2(KD_4 + C_3)(KD_2 + C_1) + 2(KD_1 + C_0) + (KD_3 + C_2)^2$
$\bar{C}$	$2(KD_4 + C_3)KD_0 + (KD_2 + C_1)^2 - 2(KD_3 + C_2)(KD_1 + C_0)$
$\bar{D}$	$2(KD_2 + C_1)KD_0 + (KD_1 + C_0)^2$
$\bar{E}$	$K^2 D_0^2$

Rearranging (22) results in the following polynomial, which is a function of ω and K:

$$f(K,\omega) = \omega^{10} + \left(\bar{A} - K^2\bar{V}\right)\omega^8 + \left(\bar{B} - K^2\bar{W}\right)\omega^6 + \left(\bar{C} - K^2\bar{X}\right)\omega^4 + \left(\bar{D} - K^2\bar{Y}\right)\omega^2 + \bar{E} - K^2\bar{Z} \geq 0, \tag{23}$$

noting that $\bar{E} - K^2\bar{Z}$ cancels out, thus reducing to the following polynomial:

$$f(K,\omega) = \omega^8 + \left(\bar{A} - K^2\bar{V}\right)\omega^6 + \left(\bar{B} - K^2\bar{W}\right)\omega^4 + \left(\bar{C} - K^2\bar{X}\right)\omega^2 + \left(\bar{D} - K^2\bar{Y}\right) \geq 0, \tag{24}$$

letting $z = \omega^2$, this results in the final optimisation polynomial:

$$f(K,z) = z^4 + \left(\bar{A} - K^2\bar{V}\right)z^3 + \left(\bar{B} - K^2\bar{W}\right)z^2 + \left(\bar{C} - K^2\bar{X}\right)z + \left(\bar{D} - K^2\bar{Y}\right) \geq 0. \tag{25}$$

In order to yield the optimal K from Equation (25), the optimisation problem requires an important selection of ω to yield the correct quadratic equation in K. The correct selection of ω is achieved by finding the frequency of the dominant resonant poles of the controlled system and the damping ratio of the controlled system in question. Once these are found, they can be substituted into Equation (25), which will yield the correction optimisation problem for K and, hence, the correct choice of K. This will be shown in detail for each controller type in this paper. Moreover, in the following section, the open–loop system is generated from experimentally sourced frequency response data based on the nanopositioner system at the University of Aberdeen [16].

3. Experimental Validations

A detailed model of the nanopositioner axis is established from experimental frequency response data (FRD) from the University of Aberdeen's nanopositioner [15,16]. The model consists of the combination of four–second–order resonance models for each significant mode in the experimental system, one first–order low pass filter for the amplifier in the experimental setup, another first–order low pass filter for the sensor measuring the experimental setup, a second–order Padé model to account for the small time delay in the system and lastly, a Bouc–Wen hysteresis model.

Considering the following graph of the FRD model of the experimental setup and the matched model, the Figure 2 summarises the FRD and the developed model:

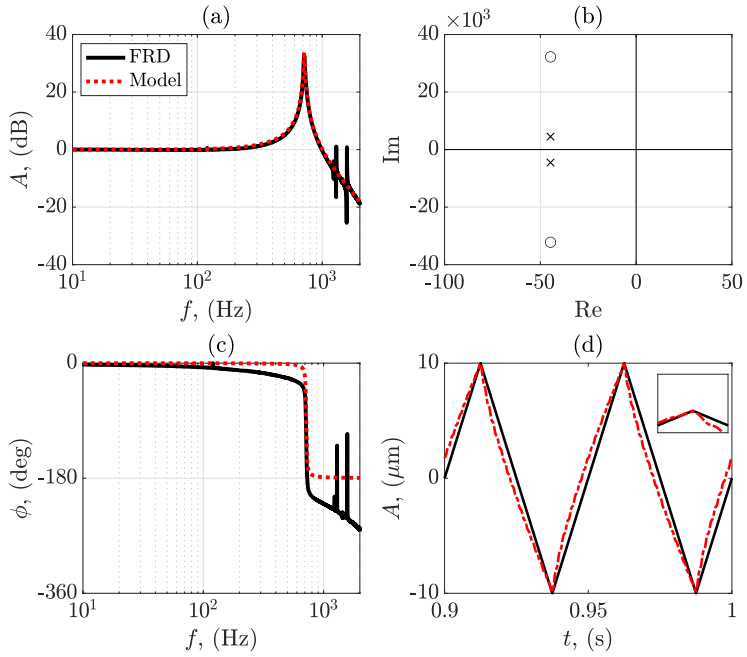


Figure 2. (**a**) The frequency amplitude response of the FRD and the developed second–order model. (**b**) The phase response of the FRD and model, respectively. (**c**) The pole-zero map of the second–order model. (**d**) represent the input signal, input signal and system response overlayed and the step response, respectively. The following table summarises the second–order model fitted to the FRD.

The second–order model detailed in Table 5 sufficiently captures the main important dynamics of the FRD model. It must be noted that only the first primary resonant mode is used for controller optimisation, as this is the primary mode at fault for the majority of oscillations. Once the optimal controller is produced, it is then subsequently simulated on the experimental model based on the FRD. In the following section, PPF control is investigated and optimised in detail subject to the aforementioned.

Table 5. Identified model details.

Coeff	Parameter	Value (s)
f_1	Mode Frequency	718 Hz
ζ_1	Damping Ratio	0.0991
γ_1^2	Numerator Constant	9×10^6
d_{f1}	Feed–Through Term	0.02
f_{amp}	Cut–Off Frequency	5000 Hz

4. PPF Optimisation and Analysis

To begin with optimising PPF control, the matrix system of Equation (12) needs to be reduced accordingly. Setting Γ_0 and Γ_1 to zero in this system will yield the PPF controller. The optimal controller vector of variables reduces to that of $\bar{\Gamma} \in \mathbb{R}^{3\times1}$ such that:

$$\bar{\Gamma} = \begin{bmatrix} \Gamma_2 \\ \Gamma_3 \\ \Gamma_4 \end{bmatrix}. \tag{26}$$

This results in the first column of $A \in \mathbb{R}^{4\times4}$ being eliminated to result in a derived matrix $\bar{A} \in \mathbb{R}^{4\times3}$, as well as $\bar{C} \in \mathbb{R}^{4\times1}$ modifying its contents. This results in the following derived system of equations:

$$\begin{bmatrix} 0 & 1 & 0 \\ -d_{f1} & 2\zeta_1\omega_1 & 1 \\ -2\zeta_1\omega_1 d_f & \omega_1^2 & 2\zeta_1\omega_1 \\ -\left(d_{f1}\omega_1^2 + \gamma_1^2\right) & 0 & \omega_1^2 \end{bmatrix} \begin{bmatrix} \Gamma_2 \\ \Gamma_3 \\ \Gamma_4 \end{bmatrix} = \begin{bmatrix} C_1 - 2\zeta_1\omega_1 \\ C_2 - \omega_1^2 \\ C_3 \\ C_4 \end{bmatrix}. \tag{27}$$

At this point, it is highly important to note a key feature of matrix Equation (27). This system of equations is overdetermined and features more equations than unknowns. Mathematically speaking, there are four equations and three unknowns, giving rise to multiple solutions for this system. Practically speaking, this will manifest in the form of having two DC gain options for a single damping ratio chosen. A system such as this can be solved approximately by utilising the method of least squares; however, this is not necessary in this case to demonstrate PPF behaviour with respect to closed–loop damping. The co-existence of solutions can be demonstrated without least squares and can be graphically demonstrated by pushing the poles of the closed–loop system further into the left–hand–plane. For all results hereafter, the DC gain is computed from Equation (7), and the error e is simply the reference subtracted from the output. Consider the following group of simulations detailing the closed–loop behaviour of PPF control.

For the optimisation procedure of PPF control, the system of equations in (27) is used with the dominant resonant mode system values of ω_1, ζ_1, γ_1^2 and d_1, respectively. The poles of the closed–loop system are varied such that $\{\sigma_d \in [-10, -9000], \omega_d = \omega_1\}$. In Figure 3a, each point on the optimisation curve represents an optimal PPF controller for the specified ω_d. The optimisation curve has two key sections that make up the whole closed–loop curve, namely the blue dashed and red solid curves, respectively. As the poles move from $\{\sigma_d = -10 \rightarrow \sigma_d = -2.70833\times10^3\}$, this represents the blue dashed curve in which the PPF controller reaches its maximum possible damping of $\zeta_{PPF} = 0.2171$. This curve also corresponds to the low DC gain that is possible for a given damping ratio. At this key value, no more extra damping of the closed–loop system is possible, and it is rendered as the final 'optimal point' in terms of just damping. As the poles move from $\{\sigma_d = -2.70833\times10^3 \rightarrow \sigma_d = -9\times10^3\}$, this represents the red solid curve in which the PPF controller travels back across the same achieved closed–loop damping values but notably possesses higher DC gain for the same damping than the blue dashed curve. The difference between the upper and lower curves in terms of their DC gains matters greatly for tracking control but not for pure damping. Figure 3(Ib) shows the difference between the obtained closed–loop damping, which is colour coded and noted in Figure 3(Ia), and the desired closed–loop damping is in solid black. Due to the PPF optimisation problem being that of an over defined one in terms of the system of equations, this does not allow for complete pole–placement. This causes the desired damping and actual obtained closed–loop damping to differ hugely, as confirmed in Figure 3(Ib). If damping is the only application required for PPF control, then selecting the maximum damping on the closed–loop optimisation curve will yield the best results; however, for tracking control, more needs to be considered. Simulation sets II and III show in detail the differences that can be found in tracking performance based on the DC gain of the PPF controller.

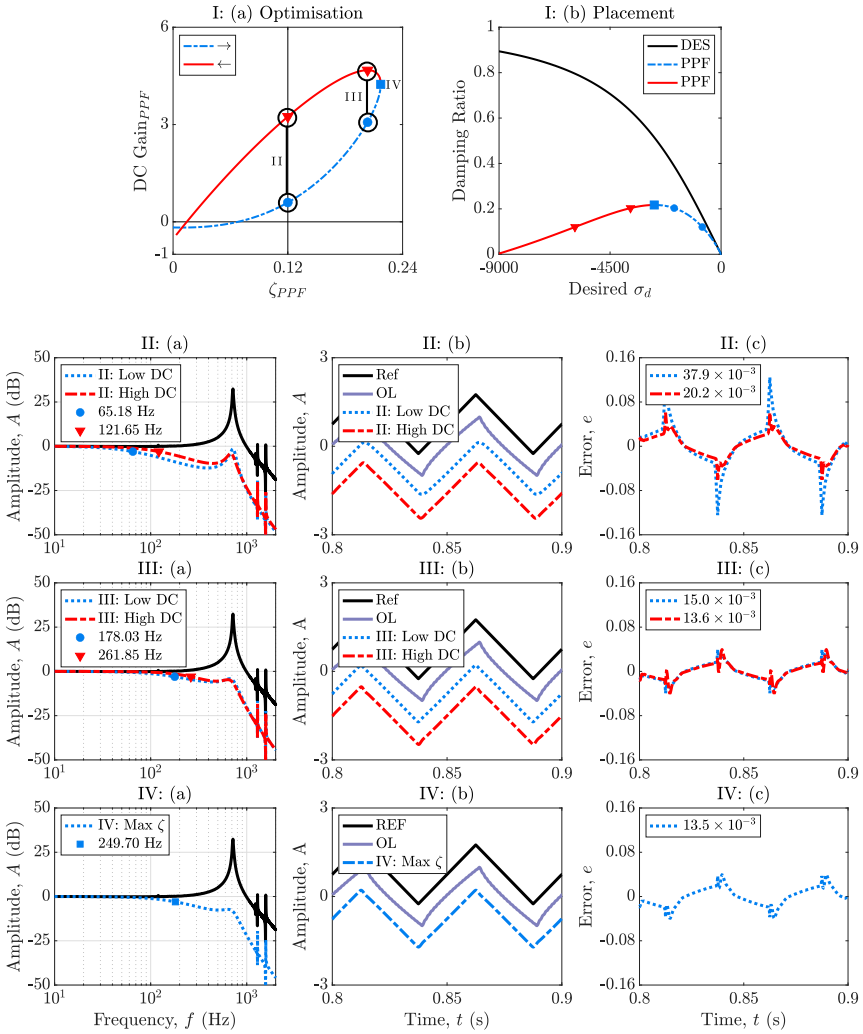


Figure 3. The PPF optimisation curve, shown by **I**: (**a**), in the middle acts as the center figure for the simulation sets (**II–IV**). **I**: (**b**) shows the desired pole location versus damping ratio for the PPF controller. Simulation sets (**II–III**) correspond to the closed–loop damping values of $\zeta_{PPF} = [0.12, 0.2034]$, respectively, and then at each point, the PPF controlled system is put in a closed–loop with an integral tracker. For each set of simulations, the damped and tracked bode plot, triangle wave time history and error plots are considered for each possible plot on the solid and dashed sections of the optimisation curve. **I**: (**a**,**b**) represent the PPF optimisation curve and the desired and PPF pole–placement curves respectively. Key points are marked on **I**: (**a**) at $\zeta_{\text{PPF}} = [0.12, 0.2034, 0.217]$. Sub figures (**II–IV**): (**a–c**) consist of each Bode responses, time histories and error plots respectively. **II**: (**a–c**) correspond to simulations taken at $\zeta_{\text{PPF}} = 0.12$, with **III**: (**a–c**) at $\zeta_{\text{PPF}} = 0.2034$ and **IV**: (**a–c**) a $\zeta_{\text{PPF}} = 0.217$ respectively.

In simulation sets II through IV, an optimal tracker is fitted to each PPF controller using Equations (17)–(25). In Figure 3(IIa–c), two PPF controllers are derived at the same damping ratio of $\zeta_{PPF} = 0.12$ with different DC gains of $G_{PPF} = 3.241$ dB and $G_{PPF} = 0.5967$ dB, respectively. In Figure 3(IIa), the low and high DC gain -3.01 dB bandwidths are $f_l \approx 70.19$ Hz and $f_h = 103.72$ Hz, respectively. Figure 3(IIb,c) show the difference in tracking the 20 Hz triangle wave and confirms that the higher DC gain PPF controller has a lower closed–loop error when compared with the lower DC gain PPF controller. The RMS errors of the low and high DC controllers are that of $e_L = 0.1681$ and $e_h = 0.1290$, respectively. A similar result is also found in Figure 3(IIIa–c)-3.01 dB, where the bandwidths are $f_l \approx 139.75$ Hz and $f_h = 198.55$ Hz, respectively. Further notice that increasing the RMS errors of the low and high DC controllers are that of $e_L = 0.1008$ and

$e_h = 0.0841$, respectively, the difference in which is the low and high DC gain. This is a key result with respect to tracking applications that also require damping. The higher the frequency is for the -3.01 dB point, the smaller the closed–loop tracking error is. As such, in a tracking application involving PPF, the higher DC gain at a specific damping ratio should always be selected. Overall, due to PPF not providing complete pole–placement, this control scheme is not recommended for both damping or damping and tracking applications. The next section considers PVPF control as a superior solution to PPF's shortcomings.

5. PVPF Optimisation and Analysis

To begin with optimising PVPF control, the matrix system of Equation (12) needs to be reduced accordingly. Setting Γ_0 to zero in this system will yield the PVPF controller and, hence, the following derived system of equations:

$$\begin{bmatrix} -d_{f1} & 0 & 1 & 0 \\ -2\zeta_1\omega_1 d_{f1} & -d_{f1} & 2\zeta_1\omega_1 & 1 \\ -\left(d_{f1}\omega_1^2 + \gamma_1^2\right) & -2\zeta_1\omega_1 d_{f1} & \omega_1^2 & 2\zeta_1\omega_1 \\ 0 & -\left(d_{f1}\omega_1^2 + \gamma_1^2\right) & 0 & \omega_1^2 \end{bmatrix} \begin{bmatrix} \Gamma_1 \\ \Gamma_2 \\ \Gamma_3 \\ \Gamma_4 \end{bmatrix} = \begin{bmatrix} C_1 - 2\zeta_1\omega_1 \\ C_2 - \omega_1^2 \\ C_3 \\ C_4 \end{bmatrix}. \quad (28)$$

Unlike in the PPF case, it is highly important to note a key feature of matrix equation (27). This system of equations is determined and features the same amount of equations and unknowns. Mathematically speaking, there are four equations and four unknowns giving rise to singular solutions for this system for a specific damping ratio, unlike in the PPF case with the co-existence of solutions. The result of having a determined system of equations in PVPF control is that pole–zero–placement is practically possible, unlike in the case of PPF control. Consider the following group of simulations detailing the closed–loop behaviour of PVPF control.

For the optimisation procedure of PVPF control, the system of Equation in (27) is used with the dominant resonant mode system values of ω_1,, ζ_1, γ_1^2 and d_1, respectively. The poles of closed–loop system are varied such that $\{\sigma_d \in [-10, -30, 000], \omega_d = \omega_1\}$. In Figure 4(Ia), the graph of the DC gain versus closed–loop damping is shown. Due to pole–placement being possible with PVPF control, unlike in PPF control, singular unique DC gains are found for each damping ratio considered. This is a direct result of PVPF control providing a determined system of equations. Figure 4(Ib) confirms pole–placement as the desired curve in solid black aligns with the closed–loop blue dashed PVPF line.

In simulation sets II through IV, an optimal tracker is fitted to each PVPF controller using Equations (17)–(25). Figure 4(IIa–c) shows the behaviour of the PVPF controller at the maximum DC gain point located at a damping ratio of $\zeta_{PVPF} = 0.63$. The -3.01 dB bandwidth is located at $f = 715.70$ Hz and results in an rms error of $e = 9.1\times10^{-3}$ when the reference and closed–loop output are phase compensated. When looking at Figure 4(IIa–c), the -3.01 dB bandwidth shifts down to $f = 559.56$ Hz, but the rms error decreases overall to $e = 4.7\times10^{-3}$ due to the extra damping imparted, namely $\zeta_{PVPF} = 0.891$. This shows that there is a substantial difference in rms error and, hence, tracking performance between II and III, which is notable. Figure 4(IVa–c) show that by going into the negative DC gain, the -3.01 dB bandwidth shifts to $f = 770.89$ Hz. This results in the rms error reducing to $e = 2.2\times10^{-3}$. To further understand PVPF's limits, examining the closed–loop response and limits of stability as the damping increases are necessary. The following figure covers the aforementioned concerns:

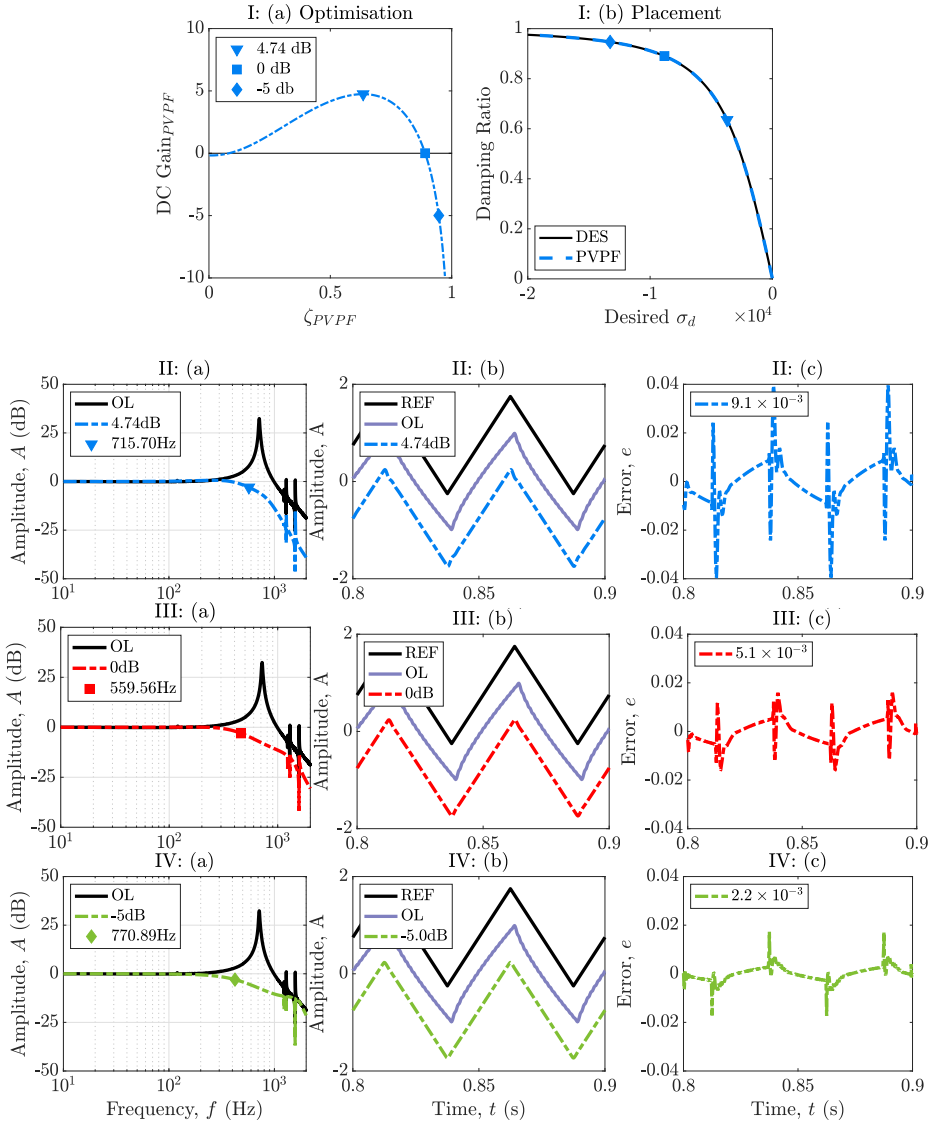


Figure 4. The PVPF optimisation curve (**I**): (**a**) shows how for a determined system of equations, only singular solutions exist for a single damping ratio. Simulation set (**I**) shows the DC gain vs. closed–loop damping ratio and pole–placement in PVPF control. Simulation sets (**II**–**IV**) correspond to the closed–loop damping values of $\zeta_{PVPF} = [0.63, 0.891, 0.947]$, respectively, and then at each point, the PVPF–controlled system is put in a closed–loop with an integral tracker. For each set of simulations, the damped and tracked bode plot, triangle wave time history and error plots are considered for each possible plot on the solid and dashed sections of the optimisation curve. **I**: (**a**,**b**) represent the PVPF optimisation curve and the desired and VPF pole–placement curves respectively. Key points are marked on **I**: (**a**) at DC $\text{Gain}_{\text{PVPF}} = [4.74, 0, -5]$. Sub figures (**II**–**IV**): (**a**–**c**) consist of each Bode responses, time histories and error plots respectively. **II**: (**a**–**c**) correspond to simulations taken at a DC gain of 4.74dB, with **III**: (**a**–**c**) at a DC gain of 0dB and **IV**: (**a**–**c**) at aDC gain of -5dB, respectively. As before, an integral tracker is fitted to each controller highlighted in **I**: (**a**).

Figure 5b,c highlights the downsides of pushing the damping up to the natural limit before instability. By going beyond and into negative DC gain PVPF controllers, the damping of the primary resonant mode becomes better as expected, but this comes at the downside of raising the closed–loop system response near other system modes. As a result, this can negatively affect impulse and step responses as well as signal tracking for frequencies in and around these system modes. Three controllers, namely, $C_1 = [0.89, 0\,\text{dB}]$, $C_2 = [0.95, -6\,\text{dB}]$ and $C_3 = [0.98, -12\,\text{dB}]$, are represented by solid black (square mark), dashed-dotted blue

(inverted triangle) and dashed lavender (diamond), respectively. The PVPF controller C_3, which is near the unstable point calculated, highlights this feature in which its amplitude response raises well above the 0 dB point for frequencies beyond the main resonance. This has the negative consequence of affecting the settling time greatly in the case of step and impulse responses as these signal types invoke infinitely many frequencies in their inception, thereby exciting these higher frequency dynamics that have been put above the crucial 0 dB point. C_3 also demonstrates a key piece of behaviour, namely that a new resonance is introduced into the system at 2028 Hz. By forcing the system too much, the closed–loop dynamics change significantly. The controller C_2 does not suffer from these effects nearly as much as in the C_3 case because it does not raise the higher frequency dynamics to be above that of the 0 dB point. The settling time between the two controllers C_1 and C_2 is comparable; however, there is more oscillatory behaviour in the step response between these two found in that of C_2; this is due to the fact that C_2 raises the higher frequency components above the primary damped resonance, albeit these frequencies are still under the critical 0 dB point.

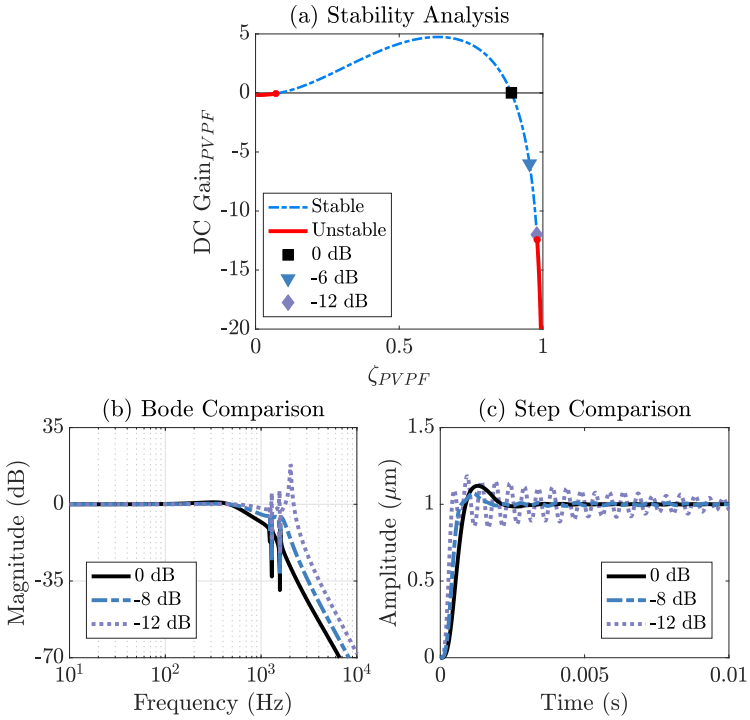


Figure 5. Figure 4a shows a graphical representation of the viable PVPF controllers when put in a closed–loop with a system. There exist three branches of stability, namely, Ξ_1, Ξ_2 and Ξ_3. Branch one, represented by a red solid line, exists such that $\{\Xi_1 \in \mathbb{R} | \Xi_1 \in (-\infty, 0.0708]\}$ and is unstable, branch two, represented by a blue dashed line, exists such that $\{\Xi_2 \in \mathbb{R} | \Xi_2 \in (0.0708, 0.9800)\}$ and is stable and lastly, branch three, represented by a red solid line, exists such that $\{\Xi_3 \in \mathbb{R} | \Xi_3 \in [0.9800, \infty)\}$ and is unstable. (**b**,**c**) shows the behaviours of the amplitude response and step responses of three key PVPF controllers found at 0 dB, -6 dB and -12 dB, respectively, from (**a**) when in closed–loop with the integral tracker.

6. PAVPF Part I: Optimisation and Analysis

In this section, PAVPF control is simulated and discussed in detail. Comparisons with PVPF are drawn directly, and a complete understanding is reached with respect to PAVPF control. To begin with optimising PAVPF control, the original derived system of Equation (12) is used directly. Unlike in the PVPF case, it is highly important to note a key feature of matrix Equation (28). This system of equations is underdetermined and features fewer equations than unknowns. Unlike in the case of PPF, which is also underdetermined, complete pole–placement is achievable with PAPVF control due to the system of

Equation (12) being an augmented PVPF problem. To this end, due to the time and bode responses found in PVPF being effectively the same as the ones that would be found with PAVPF, only comparisons with the DC gain versus damping graphs, as seen in Figure 4(Ia), are required. Consider the following simulations:

In Figure 6, PAVPF's DC gain versus closed–loop damping is considered as per Γ_0 and its subsets defined in the figure caption. Figure 6c–f provide the individual responses found for the comparisons between them in Figure 6a,b. The ranges for Γ_0 are chosen arbitrarily in order to demonstrate the nature of overdetermined PAVPF when compared with PVPF and to further demonstrate how changing the range of possible Γ_0 can affect optimal damping solutions. Figure 6c is the same PVPF curve as defined before and is used for baseline comparisons. Figure 6d–f show PAVPF with the full range of defined Γ_0, a restricted range of Γ_0 for positive reals and lastly, another restricted range for negative reals starting at -1 to the same upper bound defined in Γ_0. Figure 6d shows that with a generous range of values for Γ_0, a zig-zag pattern between DC gain and closed–loop damping is observed throughout the whole response as the poles are pushed further into the left-hand-plane subject to $\{\sigma_d \in [-10, -40, 000], \omega_d = \omega_1\}$. This zig-zag pattern's maximum and minimum DC gain decreases as the damping increases all the way up to a maximum damping of $\zeta \approx 0.949$ in which, after this point, the DC gain goes negative in a similar fashion with PVPF when the poles are pushed further. Figure 6e shows the effects of limiting the Γ_0 to only positive reals. This figure traces out a curve identical to that of PVPF up until the critical damping was found to be $\zeta \approx 0.893$. When compared with Figure 6d, this directly implies that negative Γ_0 values are found to be optimal before this key damping value, and since Figure 6e has no negative Γ_0 values, the optimisation curve is forced to follow that of the PVPF curve up to the aforementioned damping. Figure 6f confirms this as well since it allows for the use of small negative Γ_0 values down to -1 and upwards, and it follows a trajectory similar to that of Figure 6d up until a damping value of $\zeta \approx 0.564$ in which it branches off and follows a path defined by the last optimal Γ_0 found here and rejoins the other curves at the critical damping of $\zeta \approx 0.879$. The common theme between all PAVPF curves is at they all rejoin at the closed–loop damping of $\zeta \approx 0.893$ for an optimal $\Gamma_0 = 1$, and this is shown in detail in Figure 6a, which compares Figure 6d–f directly.

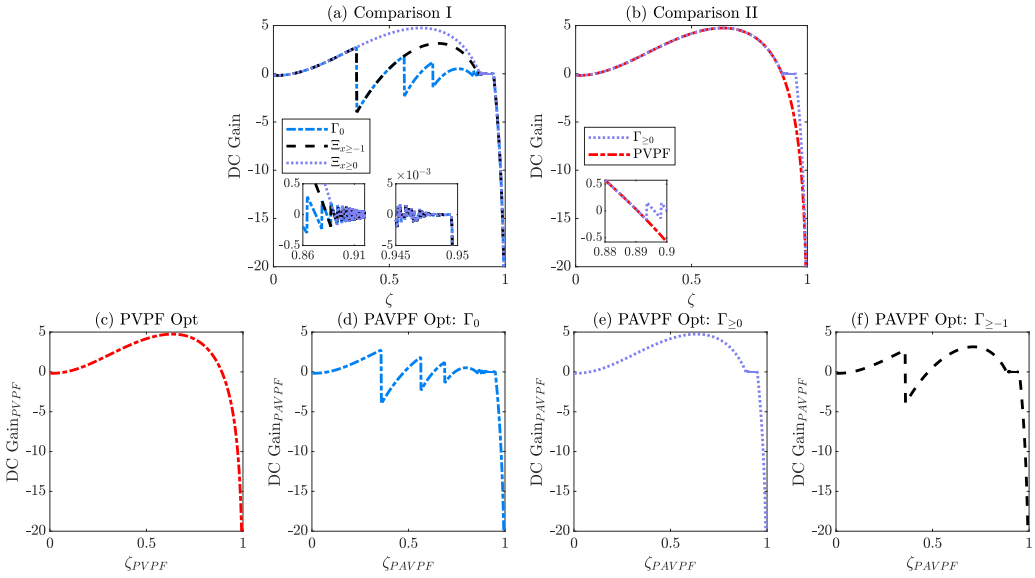


Figure 6. (**c–f**) shows the individual behaviour of three different PAVPF optimisation schemes, as well as using a PVPF optimisation curve as a baseline. (**a**,**b**) show important comparisons that infer important results about PAVPF's behaviour when subject to how it is defined in Equation (12). For (**d–f**), the Γ_0 acceleration term is iterated such that $\{\Gamma_0 \in \mathbb{R} | \Gamma_0 \in [-10,000, 10,000]\}$, $\{\Gamma_{\geq 0} \subseteq \Gamma_0 | \Gamma_{\geq 0} \in [0, 10,000]\}$ and $\{\Gamma_{\geq -1} \subseteq \Gamma_0 | \Gamma_{\geq -1} \in [-1, 10,000]\}$, respectively.

The most important conclusion that can be drawn from the PAVPF optimisation curves is namely that of Figure 6b, which compares the base PVPF with the positive real restricted PAVPF responses directly. This comparison highlights that by using PAVPF, extra damping can be achieved compared with PAVPF without going into large negative DC gain values (viz ≤ -0.2). More specifically, PVPF produces a maximum damping of $\zeta \approx 0.891$ versus the maximum damping PAVPF produces of $\zeta \approx 0.949$ without dropping into large negative DC gains. This gain in damping for the extra complexity of PAVPF on a second–order model is not worth it, given that the closed–loop time histories will be virtually identical and also the drop in the closed–loop tracking error would also not be greatly improved either. As a result, to better utilise PAVPF and understand its effects, it must be applied to a third–order system instead of a second–order one in order to avoid the underdetermined nature of system (12). The following section deals with the optimisation of PAVPF on a third–order system to address these concerns.

7. Pavpf Part II: Adapting the Problem

Since the PAVPF controller is underdetermined, as discussed earlier, a third–order model is required in order to produce proper pole–placement and meet the condition of a properly determined system. Consider the following third–order model:

$$\check{G}(s) = \frac{\omega_f}{s+\omega_f}\left(\frac{\gamma_1^2}{s^2+2\zeta_1\omega_1 s+\omega_1^2}+d_{f1}\right), \tag{29}$$

where ω_f is the cut–off frequency of a first–order filter. This first–order filter can represent sensor dynamics or amplifier dynamics that do not scale or affect the DC gain of the plant in question and are effectively part of the whole system in question. As a result, the following closed–loop system is defined as follows:

$$\check{G}_{\mathrm{CL}}(s) = \frac{\check{G}(s)}{1-\check{G}(s)C(s)_{\mathrm{PAVPF}}}. \tag{30}$$

This closed–loop system has the following DC gain function:

$$G_{dB} = 20\log_{10}\left(\frac{\left(d_{f1}\omega_1^2+\gamma_1^2\right)\Gamma_4}{\omega_1^2\Gamma_4-\left(d_{f1}\omega_1^2+\gamma_1^2\right)\Gamma_2}\right). \tag{31}$$

Notice that this function, unlike in Equation (15), is not dependent on Γ_0 due to the third–order system being used for pole–placement purposes. The denominator coefficients for Equation (30) can be seen in Table 6 as follows.

Table 6. Denominator coefficient table.

Coeff	Terms
D_4	$\Gamma_3-\omega_f d_{f1}\Gamma_0+2\zeta_1\omega_1+\omega_f$
D_3	$\Gamma_4+\left(2\zeta_1\omega_1+\omega_f\right)\Gamma_3-\omega_f d_{f1}\Gamma_1-2\zeta_1\omega_1\omega_f d_{f1}\Gamma_0+2\zeta_1\omega_1\omega_f+\omega_1^2$
D_2	$\left(2\zeta_1\omega_1+\omega_f\right)\Gamma_4+\left(2\zeta_1\omega_1\omega_f+\omega_1^2\right)\Gamma_3-\omega_f d_{f1}\Gamma_2-2\zeta_1\omega_1\omega_f d_{f1}\Gamma_1-\omega_f\left(d_{f1}\omega_1^2+\gamma_1^2\right)\Gamma_0+\omega_f\omega_1^2$
D_1	$\left(2\zeta_1\omega_1\omega_f+\omega_1^2\right)\Gamma_4+\omega_f\omega_1^2\Gamma_3-2\zeta_1\omega_1\omega_f d_{f1}\Gamma_2-\omega_f\left(d_{f1}\omega_1^2+\gamma_1^2\right)\Gamma_1$
D_0	$\omega_f\left(\omega_1^2\Gamma_4-\left(d_{f1}\omega_1^2+\gamma_1^2\right)\Gamma_2\right)$

To deal with the proper pole–placement of this system with PAVPF control, a fifth–order polynomial is required. To this end, the same poles discussed earlier are re-used, except an additional pole is introduced corresponding to the effective pole that the amplifier circuit applies to the closed–loop system:

$$\bar{P}_1, \bar{P}_2 = -\sigma_d \pm j\omega_d, \quad \bar{P}_3, \bar{P}_4 = -\sigma_d \pm j\omega_d, \quad \text{and} \quad \bar{P}_5 = -\omega_f. \tag{32}$$

Then the desired characteristic polynomial $\bar{P}_d(s)$ that has the roots given by Equation (32) is defined as:

$$\bar{P}_d(s) = s^5 + D'_{d4}s^4 + D'_{d3}s^3 + D'_{d2}s^2 + D'_{d1}s + D'_{d0}, \tag{33}$$

where the desired coefficients can be seen in Table 7.

Table 7. Desired fifth–order polynomial coefficients.

Coefficient	Expression
D'_{d4}	$\omega_f + 4\sigma_d$
D'_{d3}	$6\sigma_d^2 + 2\omega_d^2 + 4\sigma_d\omega_f$
D'_{d2}	$4\sigma_d(\sigma_d^2 + \omega_d^2) + \omega_f(6\sigma_d^2 + 2\omega_d^2)$
D'_{d1}	$(\sigma_d^2 + \omega_d^2)^2 + 4\sigma_d\omega_f(\sigma_d^2 + \omega_d^2)$
D'_{d0}	$\omega_f(\sigma_d^2 + \omega_d^2)^2$

In order to perform pole–placement between the desired polynomial (33) and the coefficients defined in Table 7, they are set equal to one another as follows;

$$D_0 = D'_{d0}, \quad D_1 = D'_{d1}, \quad D_2 = D'_{d2}, \quad D_3 = D'_{d3} \quad \text{and} \quad D_4 = D'_{d4}. \tag{34}$$

As before, this allows for a determined system of matrix equations to be generated as follows:

$$Q\check{\Gamma} = D', \tag{35}$$

where $Q^{5\times5}$, $\check{\Gamma}^{5\times1}$ and $D'^{5\times1}$, respectively. Q, $\check{\Gamma}$ and D' are as follows;

$$Q = \begin{bmatrix} -\omega_f d_{f1} & 0 & 0 & 1 & 0 \\ -2\zeta_1\omega_1\omega_f d_{f1} & -\omega_f d_{f1} & 0 & 2\zeta_1\omega_1 + \omega_f & 1 \\ -\omega_f\left(d_{f1}\omega_1^2 + \gamma_1^2\right) & -2\zeta_1\omega_1\omega_f d_{f1} & -\omega_f d_{f1} & 2\zeta_1\omega_1\omega_f + \omega_1^2 & 2\zeta_1\omega_1 + \omega_f \\ 0 & -\omega_f\left(d_{f1}\omega_1^2 + \gamma_1^2\right) & -2\zeta_1\omega_1\omega_f d_{f1} & \omega_f\omega_1^2 & 2\zeta_1\omega_1\omega_f + \omega_1^2 \\ 0 & 0 & -\omega_f\left(d_{f1}\omega_1^2 + \gamma_1^2\right) & 0 & \omega_f\omega_1^2 \end{bmatrix}, \tag{36}$$

and

$$\check{\Gamma} = \begin{bmatrix} \Gamma_0 \\ \Gamma_1 \\ \Gamma_2 \\ \Gamma_3 \\ \Gamma_4 \end{bmatrix} \quad \text{and} \quad D' = \begin{bmatrix} D'_{d0} - \omega_f - 2\zeta_1\omega_1 \\ D'_{d1} - \omega_1^2 - 2\zeta_1\omega_1\omega_f \\ D'_{d2} - \omega_f\omega_1^2 \\ D'_{d3} \\ D'_{d4} \end{bmatrix}. \tag{37}$$

In the following comparison, the amplifier sensor's cut–off frequency $\omega_f = 10,000\pi$ is used as the additional pole introduced in this third–order system. Consider the following comparison in Figure 7.

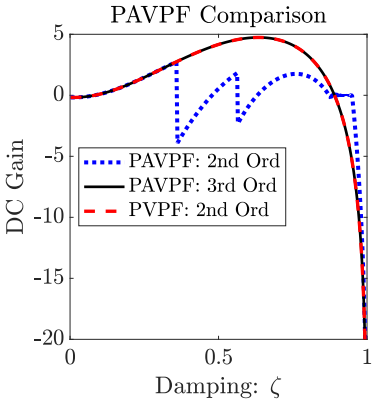


Figure 7. This figure details the comparison of PVPF (red dashed) and PAVPF (blue dotted) designed on the second–order system compared with PAVPF (black solid) designed on the third–order system in order to force proper conditioning of PAVPF.

By properly conditioning PAVPF control on a third–order system as defined previously, this produces a virtually identical optimisation curve when compared with PVPF control on the second–order system as seen in Figure 7. PAVPF implemented on the second–order system, which is overdetermined, allows for extra damping while keeping the DC gain close to zero. As a result, even though time histories would not show much difference between $\zeta \approx 0.891$ and $\zeta = 0.949$ on PAVPF determined and PAVPF overdetermined, overdetermined PAVPF still provides more possible damping while keeping the DC gain close to zero. This implies that overdetermined PAVPF is more optimal for damping versus determined PAVPF, which also includes damping with tracking as well.

8. Concluding Remarks

This paper addresses a long–standing knowledge gap with respect to a second–order damping system and how far to push the closed–loop poles of the system in question, as well as addressing the concept of determined, underdetermined and overdetermined optimisation problems with respect to pole–placement. Since PAVPF control encodes PVPF and PPF control, respectively, the optimisation process is designed around PAVPF first. A general blueprint for PPF, PVPF and PAVPF damping optimisation is obtained by converting the pole–placement strategy into its matrix form on a second–order system. This matrix form begins in an underdetermined form due to PAVPF requiring a third–order system for proper pole–placement. Subsequent to this, PVPF and PPF pole–placement methodologies are derived from this blueprint by omitting the acceleration term as well as the acceleration and velocity terms, respectively. In the final part of the paper, a fully determined form for PAVPF is developed in a similar manner to PVPF and then analysed and compared to fully determined PAVPF and overdetermined PAVPF.

Overall, the most pivotal result is found within the comparisons between PAVPF and PVPF control when PAVPF is made to be overdetermined and fully determined. Fully determined PAVPF is virtually identical to fully determined PVPF in terms of the optimal DC gain versus the damping curve produced, and only the undetermined PAVPF optimisation procedure can produce additional damping over its regular fully determined counterpart.

Author Contributions: M.A. was responsible for the conceptualisation, methodology, formal analysis and writing–original draft. S.S.A. was responsible for conceptualisation, writing–review and editing and supervision. J.M. was responsible for formal analysis, writing–review and editing, visualistion, conceptualisation and formal analysis. All authors have read and agreed to the published version of the manuscript.

Funding: This research received no external funding.

Institutional Review Board Statement: Not applicable.

Informed Consent Statement: Not applicable.

Data Availability Statement: Not applicable.

Conflicts of Interest: The authors declare no conflict of interest.

References

1. Preumont, A. *Vibration Control of Active Structures: An Introduction*; Kluwer: Dordrecht, The Netherlands, 1997.
2. Beards, C. *Engineering Vibration Analysis with Application to Control Systems Ebook*; Butterworth-Heinemann: Oxford, UK, 1995.
3. Beards, C.F. *Structural Vibration: Analysis and Damping Ebook*; Butterworth-Heinemann: Oxford, UK, 1996.
4. Mead, D.J. *Passive Vibration Control*; Wiley: Hoboken, NJ, USA, 1999.
5. Fuller, C.R.; Elliott, S.; Nelson, P.A. *Active Control of Vibration*; Academic Press: Cambridge, MA, USA, 1997.
6. Moheimani, S.O.R.; Fleming, A.J. *Piezoelectric Transducers for Vibration Control and Damping (Advances in Industrial Control)*; Springer: Berlin/Heidelberg, Germany, 2006.
7. Preumont, A.; de Marneffe, B.; Deraemaeker, A.; Bossens, F. The damping of a truss structure with a piezoelectric transducer. *Comput. Struct.* **2008**, *86*, 227–239. [CrossRef]
8. Aphale, S.S.; Fleming, A.J.; Moheimani, S.O.R. Integral resonant control of collocated smart structures. *Smart Mater. Struct.* **2007**, *16*, 439–446. [CrossRef]
9. Balas, M.J. Direct Velocity Feedback Control of Large Space Structures. *J. Guid. Control Dyn.* **1979**, *2*, 252–253. [CrossRef]
10. Aphale, S.S.; Fleming, A.J.; Moheimani, S.O.R. High Speed Nano-scale Positioning using a Piezoelectric Tube Actuator with Active Shunt Control. *IET Micro Nano Lett.* **2007**, *2*, 9–12. [CrossRef]
11. Pota, H.R.; Moheimani, S.O.R.; Smith, M. Resonant controllers for smart structures. *Smart Mater. Struct.* **2002**, *11*, 1–8. [CrossRef]
12. Salapaka, S.; Sebastian, A.; Clevland, J.P.; Salapaka, M.V. High bandwidth nano-positioner: A robust control approach. *Rev. Sci. Instruments* **2002**, *73*, 3232–3241. [CrossRef]
13. Moheimani, S.O.R.; Vautier, B.J.G.; Bhikkaji, B. Experimental implementation of extended multivariable PPF control. *IEEE Trans. Control Syst. Technol.* **2006**, *14*, 443–455. [CrossRef]
14. Bhikkaji, B.; Ratnam, M.; Fleming, A.J.; Moheimani, S.O.R. High-Performance Control of Piezoelectric Tube Scanners. *IEEE Trans. Control Syst. Technol.* **2007**, *15*, 853–866. [CrossRef]
15. Babarinde, A.K.; Zhu, L.M.; Aphale, S.S. Simultaneous design of positive acceleration velocity and position feedback based combined damping and tracking control scheme for nanopositioners. In Proceedings of the 2019 18th European Control Conference, ECC 2019, Naples, Italy, 25–28 June 2019. [CrossRef]
16. Babarinde, A.K.; Li, L.; Zhu, L.; Aphale, S.S. Experimental validation of the simultaneous damping and tracking controller design strategy for high-bandwidth nanopositioning—A pavpf approach. *IET Control Theory Appl.* **2020,** 14, 3506–3514 . [CrossRef]
17. Bhikkaji, B.; Ratnam, M.; Moheimani, S.O.R. PVPF control of piezoelectric tube scanners. *Sens. Actuators A. Phys.* **2007**, *135*, 700–712. [CrossRef]
18. Sebastian, A.; Pantazi, A.; Moheimani, S.O.R.; Pozidis, H.; Eleftheriou, E. Achieving sub-nanometer precision in a MEMS storage device during self-servo write process. *IEEE Trans. Nanotechnol.* **2008**, *7*, 586–595. [CrossRef]
19. Wang, L. Positive position feedback based vibration attenuation for a flexible aerospace structure using multiple piezoelectric actuators. In Proceedings of the 22nd Digital Avionics Systems Conference, DASC'03, Indianapolis, IN, USA, 12–16 October 2003; Volume 2.
20. Mahmood, I.A.; Moheimani, S.O.R.; Bhikkaji, B. Precise Tip Positioning of a Flexible Manipulator using Resonant Control. *IEEE/ASME Trans. Mechatron.* **2008**, *13*, 180–186. [CrossRef]
21. Cherubini, G.; Chung, C.C.; Messner, W.C.; Moheimani, S.O.R. Control Methods in Data-Storage Systems. *IEEE Trans. Control Syst. Technol.* **2012**, *20*, 296–322. [CrossRef]
22. Aphale, S.S.; Bhikkaji, B.; Moheimani, S.O. Minimizing scanning errors in piezoelectric stack-actuated nanopositioning platforms. *IEEE Trans. Nanotechnol.* **2008**, *7*, 79–90. [CrossRef]
23. Pereira, E.; Aphale, S.S.; Feliu, V.; Moheimani, S.O. Integral resonant control for vibration damping and precise tip-positioning of a single-link flexible manipulator. *IEEE/ASME Trans. Mechatron.* **2011**, *16*, 232–240. [CrossRef]
24. Moheimani, S.O.R. Invited Review Article: Accurate and Fast Nanopositioning with Piezoelectric Tube Scanners: Emerging Trends and Future Challenges. *Rev. Sci. Instrum.* **2008**, *79*, 071101. [CrossRef] [PubMed]
25. Devasia, S.; Eleftheriou, E.; Moheimani, S.O.R. A Survey of Control Issues in Nanopositioning. *IEEE Trans. Control Syst. Technol.* **2007**, *15*, 689–703. [CrossRef]
26. Clark, R.L. Accounting for out-of-bandwidth modes in the assumed modes approach: Implications on collocated output feedback control. *Trans. ASME J. Dyn. Syst. Meas. Control* **1997**, *119*, 390–395. [CrossRef]
27. Fanson, J.L.; Caughey, T.K. Positive position feedback control for large space structures. *AIAA J.* **1990**, *28*, 717–724. [CrossRef]